Electronic Supplementary Material (ESI) for Journal of Materials Chemistry C.


# Supporting Information

# A Conceptual Framework for Designing and Analyzing Complex Molecular Circuits

Ravinder Kumar[a], Charu Seth[b], Veerabhadrarao Kaliginedi[b], Ravindra Venkatramani[a,*]

[a] Department of Chemical Sciences, Tata Institute of Fundamental Research, Mumbai-400005, India

[b] Department of Inorganic and Physical Chemistry (IPC), Indian Institute of Science, Bangalore-560012, India

## Corresponding Author

Ravindra Venkatramani (email: ravi.venkatramani@tifr.res.in)

Department of Chemical Sciences, Tata Institute of Fundamental Research, Dr. Homi Bhabha Road, Colaba, Mumbai 400005, Maharashtra, India

## S.1 Conformation Sampling Algorithm

Here, we describe an algorithm (Fig. S1) to sample the conformations of small molecules and demonstrate its working and applicability with the help of 3 simple biphenyl and para-terphenyl molecules (Fig. S2). In the main manuscript, the algorithm is applied to the TPx breadboard molecules to enumerate their initial geometries as well as obtain distinct DFT optimized structures. Our algorithm improves previous methods[1,2] by accounting for molecular symmetries while enumerating conformations to reduce the number of structures to be processed. The flowchart in Fig. S2 describes the steps of the algorithm where conformational degrees of freedom of the molecule (only dihedral angles which lead to conformational flexibility (cf-DAs)) are combined as a vector ($v$) and molecular rotational symmetries are given by rotation and translation matrices ($r \in R$, the space of all symmetry operations) operating on $v$. Note that here we consider ***molecular symmetries based on the connectivity of atoms within the molecule*** rather than the actual symmetry elements present in the molecule which get perturbed by simple dihedral rotations. Thus, $r$ are permutation matrices which are chosen such that they exchange/permute cf-DAs while maintaining the same atom connectivity graph. The matrices $r$ represent rotation of either the molecule or its fragments. A molecular rotation does not change molecular conformation but leads to a different viewing angle for an observer, which helps eliminating redundancies of identical conformations. Likewise, fragment symmetries provide a new perspective of the molecule upon rotating the fragment around the bond connecting it to the rest of the molecule by an angle related to its symmetry (for example, if a fragment has $C_2$ symmetry, a rotation of 180° keeps the conformation intact with few exchanges of cf-DAs in $v$). The dimension of $v$ is the same as the number of cf-DAs present in the molecule. The sequence of cf-DAs in $v$ determines the symmetry matrices to be constructed for the molecular rotations. Below we demonstrate the algorithm on biphenyl, para-terphenyl, and meta-terphenyl molecules possessing only 1, 2, and 2 torsional degrees of freedom respectively (Fig. S1).

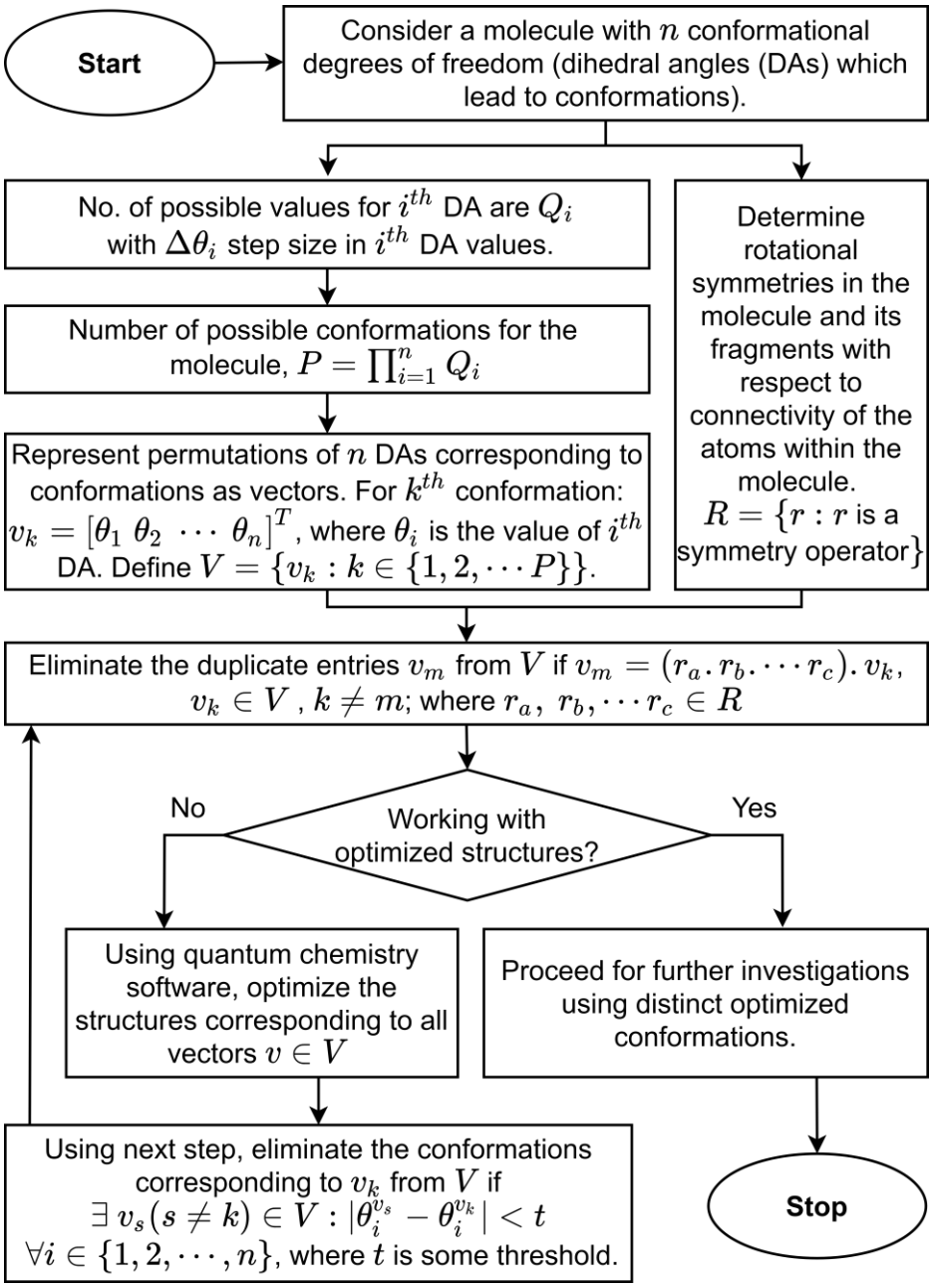


**Fig. S1:** Flowchart to enumerate conformations of the small molecules.

**Biphenyl:** Rotation about single bond connecting the two phenyl rings is the only cf-DA in biphenyl molecule ($n = 1$). With discretization $\Delta\theta_1$ =90°, $\theta_1$ (Fig. S1) can take 4 values ($Q_i = 4$; $i = 1$). With these specifics, total number of conformations possible for biphenyl are 4 ($P = 4$). The 1D conformational angle vectors are written as: $v_1 = [0]$, $v_2 = [90]$, $v_3 = [180]$, $v_4 = [270]$. Molecular rotation symmetries do not affect the angle vectors $v_1$-$v_4$. However, phenyl ring (a molecular fragment) in the molecule has $C_2$ (= $r_1$ and $r_3$ for the two phenyl rings respectively) symmetry which implies that rotation of phenyl torsion ($\equiv \theta_1$) by 180° leads to a same conformation. Thus, the rotational symmetry $r$ of the phenyl fragment is a $1 \times 1$ matrix

which translates $\theta_1$ by 180°, $r_2 = [180]$ leading to the conformations corresponding to $v_1$ and $v_2$ be identical to $v_3$ and $v_4$ respectively. Conclusively, for $\Delta\theta_1 = 90°$, symmetry elements reduce the number of conformations of biphenyl from 4 to 2 (Table S1).

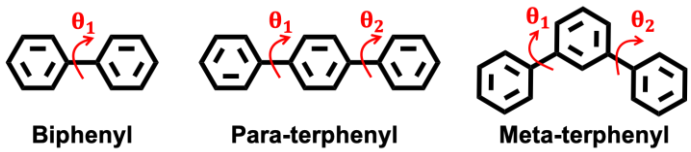


**Fig. S2:** Biphenyl, para-terphenyl, and meta-terphenyl molecules with 1, 2, and 2 conformational degrees of freedom ($\theta_1$ and $\theta_2$) by rotations about the bonds connecting two rings (red arrow).

**Para and meta-terphenyl:** There are two cf-DAs in terphenyl molecules which are torsional rotations between adjacent phenyl rings ($n = 2$). With discretization $\Delta\theta_i$ =90°, $\theta_1$ and $\theta_2$ (Fig. S1) can take 4 values ($Q_i = 4$; $i = 1,2$). With these specifics, total number of conformations

**Table S1**: Total possible and distinct conformations of three breadboard molecules. Here, $n$, $Q_i$, and $P$ are number of rotatable dihedrals, number of values for $i^{th}$ dihedral torsion, total number of possible angle vectors respectively. $D$ is number of distinct initial conformations and $D_{en}$ is number of distinct initial conformations after eliminating enantiomers.

| **Molecule** | $\boldsymbol{n}$ | $\boldsymbol{Q_i}$ | $\boldsymbol{P}$ | $\boldsymbol{R}$[(a)] | $\boldsymbol{D}$ | $\boldsymbol{D_{ren}}$ |
|---|---|---|---|---|---|---|
| Biphenyl | 1 | 4 | 4 | $r_1, r_2, r_3$ | 2 | 2 |
| Meta-terphenyl | 2 | $4, 4$ | $4^2 = 16$ | $r_1, r_2, r_3, r_4$ | 3 | 3 |
| Para-terphenyl | | | | $r_1, r_3, r_4$ | 3 | 3 |
| TPm | 6 | $4, 4, 4, 4, 4, 4$ | $4^2 = 4096$ | $r_1, r_2, r_3, r_4, r_5$ | 288 | 168 |
| TPo | | | | $r_1, r_2, r_3, r_4, r_5$ | 288 | 168 |
| TPp | | | | $r_1, r_2, r_3, r_4, r_5, r_6$ | 24 | 23 |

[(a)]Each of symmetry elements is defined in the text for corresponding molecule.

possible for terphenyls are 16 ($P = Q_1 \times Q_2 = 4^2$). Two-dimensional conformational angle vectors can be written as: $v_1 = [0,0]^T$, $v_2 = [0,90]^T$, $v_3 = [0,180]^T$, $\cdots$ $v_{16} = [270,270]$. One of the molecular rotational matrices for terphenyl molecules is a matrix which leads to exchange of $\theta_1$ and $\theta_2$:

$$r_1 = \begin{pmatrix} 0 & 1 \\ 1 & 0 \end{pmatrix} \quad \text{(S1)}$$

Other rotations include addition of rotation angle to the two-dimensional angle vector (translation of vectors by the angle of molecular rotation) for para-terphenyl. For $\Delta\theta_i = 90°$, addition of vector $r_2 = [90,90]$ to $v_1$-$v_{16}$ rotates the molecule by 90° along the line joining

three phenyl rings, $r_2^4$ ($r_2$ applied 4 times) is equal to Identity. Translation of vectors is required only when all the cf-DAs lie on a line. Therefore, for meta-terphenyl there is only one molecular rotational matrix (Eqn. S1). Moreover, the phenyl ring has $C_2$ (translations $r_3 = [0, 180]^T$ and $r_4 = [180, 0]^T$ to $v_1$-$v_{16}$ for two terminal phenyl rings respectively) symmetry which further reduces the number of conformations for the terphenyl molecules. Note that fragment symmetry ($r_3$ and $r_4$) appears as a translation of one DA around the bond connecting the fragment. Finally, by applying all symmetry elements on the vectors $v_1$-$v_{16}$, the number of conformations reduces from 16 to 3 (Table S1). Note that, in practice, we eliminate the redundant conformations by adding a new vector $v_i$ to an existing set of vectors $V$, only if symmetry operations on $v_i$ does not lead a vector $v_j \in V$.

**TPx breadboard:** In the main manuscript we present application of the algorithm to the 3 breadboard molecules (TPm, TPo, and TPp). Symmetry matrices (listed in Table 1) for the 3 breadboards are:

$$r_1 = \begin{pmatrix} 0 & 1 & 0 & 0 & 0 & 0 \\ 1 & 0 & 0 & 0 & 0 & 0 \\ 0 & 0 & 1 & 0 & 0 & 0 \\ 0 & 0 & 0 & 1 & 0 & 0 \\ 0 & 0 & 0 & 0 & 0 & 1 \\ 0 & 0 & 0 & 0 & 1 & 0 \end{pmatrix} \quad \text{(S2.)}$$

$$r_2 = \begin{pmatrix} 0 & 0 & 0 & 0 & 1 & 0 \\ 0 & 0 & 0 & 0 & 0 & 1 \\ 0 & 0 & 0 & 1 & 0 & 0 \\ 0 & 0 & 1 & 0 & 0 & 0 \\ 1 & 0 & 0 & 0 & 0 & 0 \\ 0 & 1 & 0 & 0 & 0 & 0 \end{pmatrix} \quad \text{(S3)}$$

$$r_3 = \begin{pmatrix} 0 & 0 & 0 & 0 & 0 & 1 \\ 0 & 0 & 0 & 0 & 1 & 0 \\ 0 & 0 & 0 & 1 & 0 & 0 \\ 0 & 0 & 1 & 0 & 0 & 0 \\ 0 & 1 & 0 & 0 & 0 & 0 \\ 1 & 0 & 0 & 0 & 0 & 0 \end{pmatrix} \quad \text{(S4)}$$

$$r_4 = \begin{pmatrix} 1 & 0 & 0 & 0 & 0 & 0 \\ 0 & 1 & 0 & 0 & 0 & 0 \\ 0 & 0 & 1 & 0 & 0 & 0 \\ 0 & 0 & 0 & 1 & 0 & 0 \\ 0 & 0 & 0 & 0 & 0 & 1 \\ 0 & 0 & 0 & 0 & 1 & 0 \end{pmatrix} + \text{translation of angle } \theta_4 \text{ by } 180° \quad \text{(S5)}$$

$$r_5 = \begin{pmatrix} 0 & 1 & 0 & 0 & 0 & 0 \\ 1 & 0 & 0 & 0 & 0 & 0 \\ 0 & 0 & 1 & 0 & 0 & 0 \\ 0 & 0 & 0 & 1 & 0 & 0 \\ 0 & 0 & 0 & 0 & 1 & 0 \\ 0 & 0 & 0 & 0 & 0 & 1 \end{pmatrix} + \text{translation of angle } \theta_3 \text{ by } 180° \quad \text{(S6)}$$

$r_6 = C_2$ symmetry for peripheral pyridyl rings with N-atom at para position.
$r_6$ represents the translation of DA about the bond connecting pyridyl ring to rest of molecule by 180°. (S7)

Here, $r_1$-$r_3$ are the molecular symmetry matrices, $r_4$ and $r_5$ are the fragment symmetry matrices for terpyridine arms, and $r_6$ is the fragment symmetry matrix for the peripheral pyridyl rings which possess symmetry in TPp molecule only.

## S.2 Conformational States of TPx Before and After Optimization

The terpyridine arms in TPx molecules have two peripheral pyridyl rings. The stereochemistry of the linking N-atoms in the peripheral pyridyl rings impact the conformations of the breadboard molecules. In the extreme conjugation cases adjacent rings are either in plane or perpendicular to each other. The N-atom on a peripheral ring in TPm and TPo can face towards the core N-atom (Fig. S3A) or away (Fig. S3B) when the peripheral and core rings are planar to each other. Alternatively, when peripheral and core rings are perpendicular to each other, the peripheral N-atom can either point up (Fig. S3C) or down (Fig. S3D) relative to the plane of core ring in the terpyridine arm. We start with 168, 168, 23 conformations of TPm/o/p respectivey which have extreme conjugations and then optimized them using using DFT with B3LYP exchange-correlation functional and the 6-31G* basis set in Gaussian 09 revision D.01.[3] Adjacent ring DAs ($\theta_1$-$\theta_6$) for initial conformations are shown in Fig. S4A-C. After optimization, conformations fall in certain local minima. We bin the optimized DAs ($\theta_1$-$\theta_6$) in

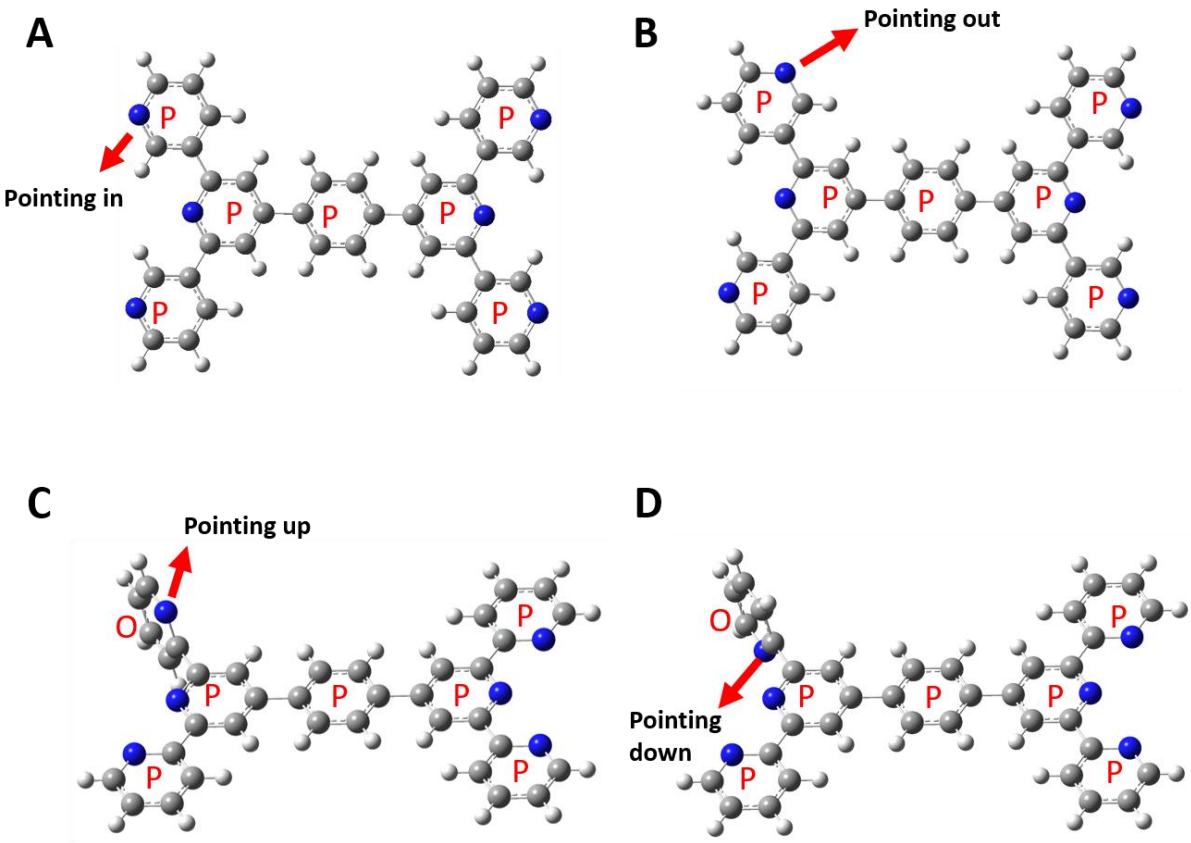


**Fig. S3:** Peripheral and core rings are: (**A**) in plane and peripheral N atom is facing towards the core N-atom (red arrow), (**B**) in plane and peripheral N atom facing away from the core N-atom (red arrow), (**C**) perpendicular to each other and peripheral N atom points up relative to core ring (red arrow), and (**D**) perpendicular to each other and peripheral N atom points down relative to core ring (red arrow).

Fig. S4D–F. The stereochemistry of N-atoms is present for optimized conformations as well, however, the angle for pointing in and out or up and down for the peripheral N-atoms changes. After optimization adjacent ring DAs between peripheral and core rings are not continuous but

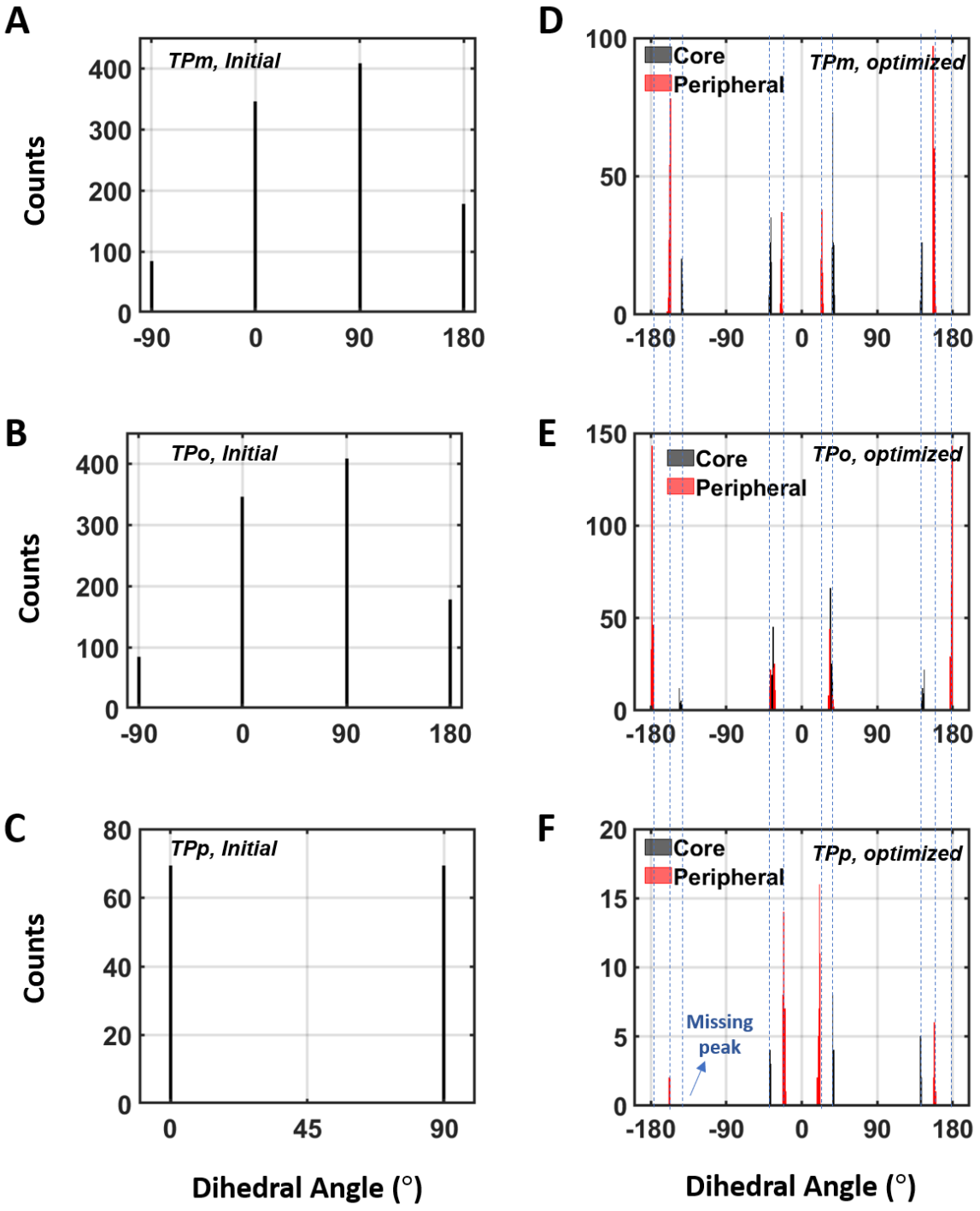


**Fig. S4:** Adjacent ring dihedral angles for initial conformations of (**A**) TPm, (**B**) TPo, and (**C**) TPp; and for the optimized conformations of (**D**) TPm, (**E**) TPo, and (**F**) TPp. The core dihedral angles lie in the same interval for optimized conformations of three breadboards allowing us to use 3rp circuit as a reference circuit (compare black bars in D-F).

rather fall in certain intervals. In an absolute sense, the angle between adjacent ring planes (*i.e.*, neglecting stereochemistry of N-atoms) are in the intervals 18-26° (peripheral DAs in TPm and TPp), 31-40° (core DAs for three molecules and peripheral DAs for a few conformations of TPo), and 1-3° (peripheral DAs for major contributing conformations of TPo which lead to almost planar terpyridine arms of TPo). Thus, *the conformations of TPm and TPp have similar dihedral angles whereas TPm and TPo differ significantly*. Further, terpyridine arms in TPo adopt more planar conformations. On the other hand, the core dihedral angles across three breadboards remain similar indicating similar conformational states for the 3rp circuit, although peak heights in Fig. S4D-F (black histograms) are different. Nonetheless, there are only two conformational states for 3rp across TPx breadboards (see section S4 for representative structures).

## S.3 Free Energies of Molecular Conformations

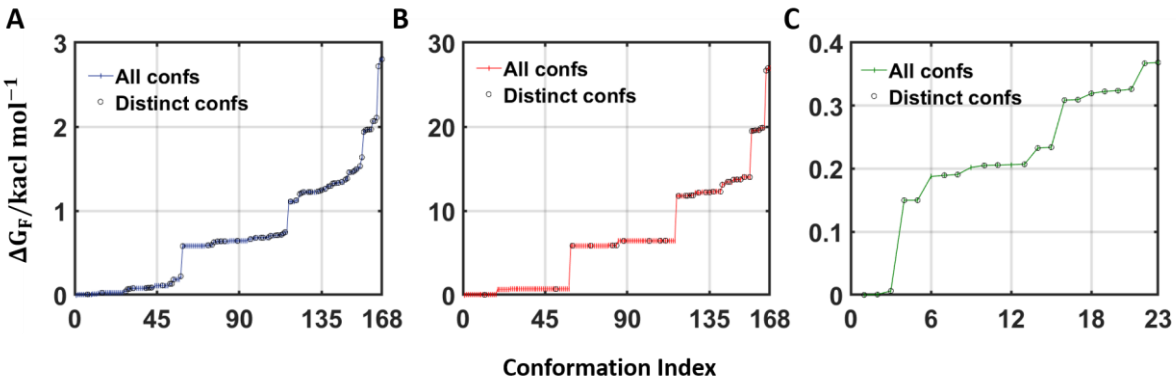


**Fig. S5:** Free energies of all optimized conformations of (**A**) TPm, (**B**) TPo, and (**C**) TPp as a function of (arbitrary) conformation index. Geometrically distinct conformations are marked by black circles.

## S.4 Multiple Conductance States for TPx Basis Circuits and the Corresponding Representative Conformations

The basis circuit conductance distributions across the three breadboards often show multiple peaks (see Figs. 2D–2F and Figs. S6–S8). For instance, the 2r circuit (blue data in Figs. 2D-2F and Figs. S6–S8) shows two ($\log(G/G_{max})$ peak values each for TPm and TPo (ca. −0.95 and −1.1 for TPm and ca. 0 and −0.1 for TPo) but only a single peak for TPp (around −0.1). Multiple peaks arise from the contributions to the circuit conductance by 12 distinct conformational

states (termed CS1–CS12) of the breadboards (Figs. S6–S8). We define these conformational states in terms of the stereochemistry of the peripheral N atoms (either pointing toward or away from the core N atom) for 2r, 3rm, 4r, and 5r circuits and the angle of the two flanking pyridyl rings (∼0° or ∼75°) relative to the central phenyl ring for 3rp circuit. Fig. S6 assigns the multiple conductance peaks (2, 3, 2, 2, and 3) for 2r–5r basis circuits in TPm to the 12 conformational states. On the other hand, the symmetric para placement of N atoms in TPp precludes distinct stereochemistry for the peripheral N atoms, and thus the 2r, 4r, and 5r circuits in this breadboard show only single peak (Fig S7). The 3rm and 3rp circuits for TPp show two conductance peaks—which, for the latter, can be assigned to CS6 and CS7. However, the two conductance peaks for 3rm circuit cannot be assigned uniquely to any of the 12 conformational states, and we present representative conformations for these peaks in Fig S7. In Fig. S8, we assign the conductance states for the TPo circuits to the conformational states. While the 3rm and 4r circuits show multiple conductance subpopulations within an assigned conformational state (CS3 and CS8, respectively), the 4r circuit shows a broad conductance distribution which cannot be assigned to any specific conformational state, and we show representative geometries. As noted earlier, not all breadboard conformations contribute significantly to the final conductance statistics. Specifically, the relative populations / peak heights in the conductance distributions in Figs. 2D–2F are influenced by the Boltzmann weights for the conformations in Figs. 2A–2C. For instance, the 2r TPo circuit (blue histogram in Fig 2E) shows two conductance peaks differing by five orders of magnitude, with the higher conductance peak ($w_i^B > 0.99$) arising from CS2 (Fig. S8) and the lower conductance peak ($w_i^B \sim 10^{-5}$) arising from CS1, (Fig. S8). On the other hand, in a 2r TPm circuit (blue histogram in Fig 2D), both states CS1 and CS2 (Fig. S6) are significantly populated ($w_i^B$ ∼0.35 and ∼0.65, respectively) leading to two conductance peaks of unequal (but comparable) heights for the 2r circuit. In contrast, the conductance of a 2r TPp circuit arises from a single conformation. Thus, this section demonstrates the complexity of the TPx breadboard conformational space and the need for a rigorous accounting of their contributions to the conductance statistics. The resultant conductance distributions shown in Figs. 2D–2F, which are obtained in the absence of REA, showcase the possibility of QIE within and across the breadboard molecules. In the main text, we portray the effect of QIE more clearly and examine the combined effect of REA and QIE for tuning the conductance distributions of the basis circuits across the three breadboard scaffolds.

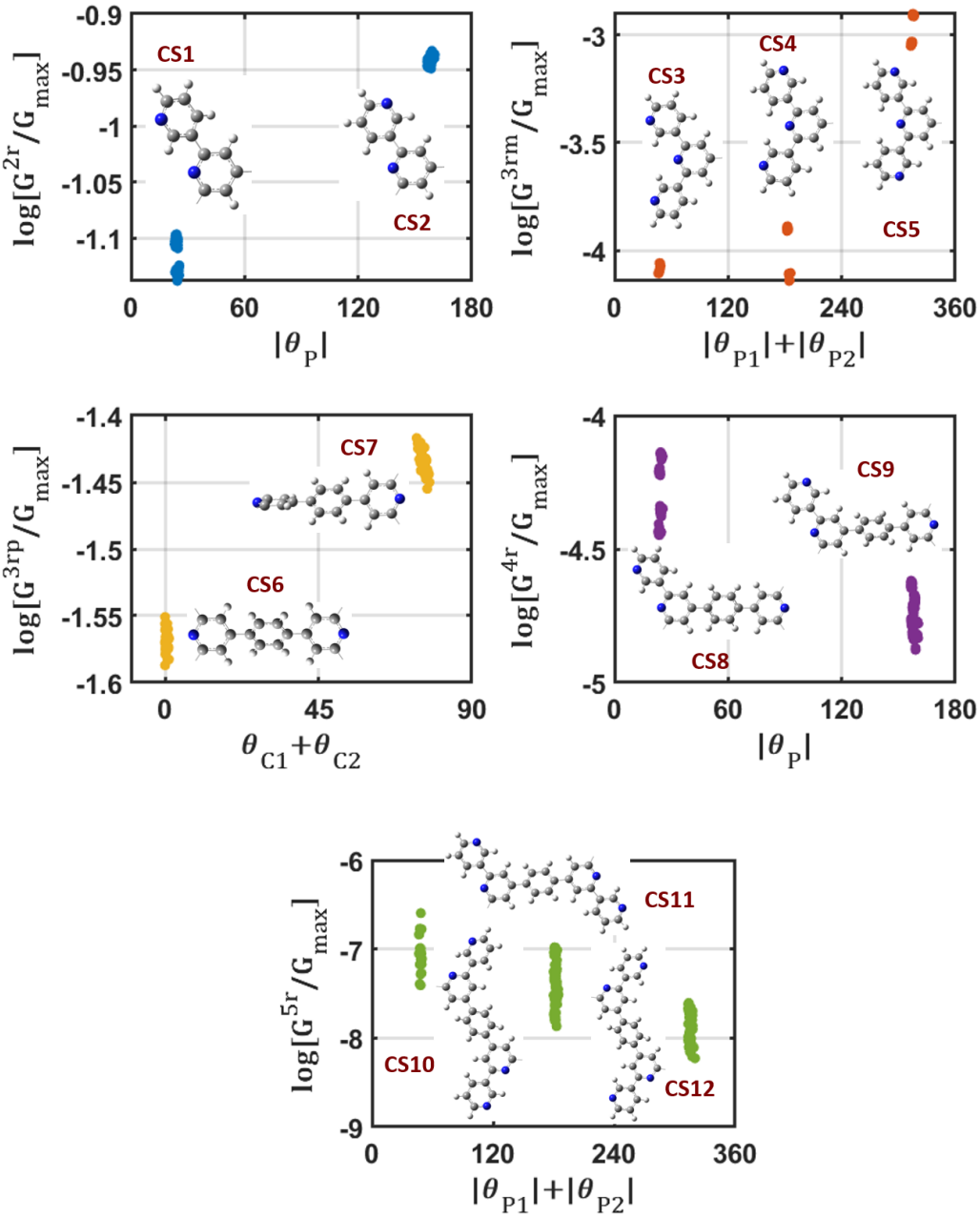


**Fig. S6:** Scatter plots for the logarithmic conductance of 5 basis circuits in all the distinct conformations of TPm. The logarithmic conductance is plotted as function of composite angles which define conformational state for a particular basis circuit. The composite angle is related to in and out conformations of peripheral N-atoms (section S2) in case of 2r, 3rm, 4r, and 5r circuits while it is related to angle between the core pyridyl rings in case of 3rp. The corresponding conformational states for basis are shown inside the plot. The multiple conductance states for basis circuits correlate well with the conformational states. However, for a few circuits multiple peaks are not resolved (for instance, 5r circuit). $\theta_P$, $\theta_{P1}$, $\theta_{P2}$, $\theta_{C1}$, and $\theta_{C2}$ are the dihedral angles for the corresponding circuit.

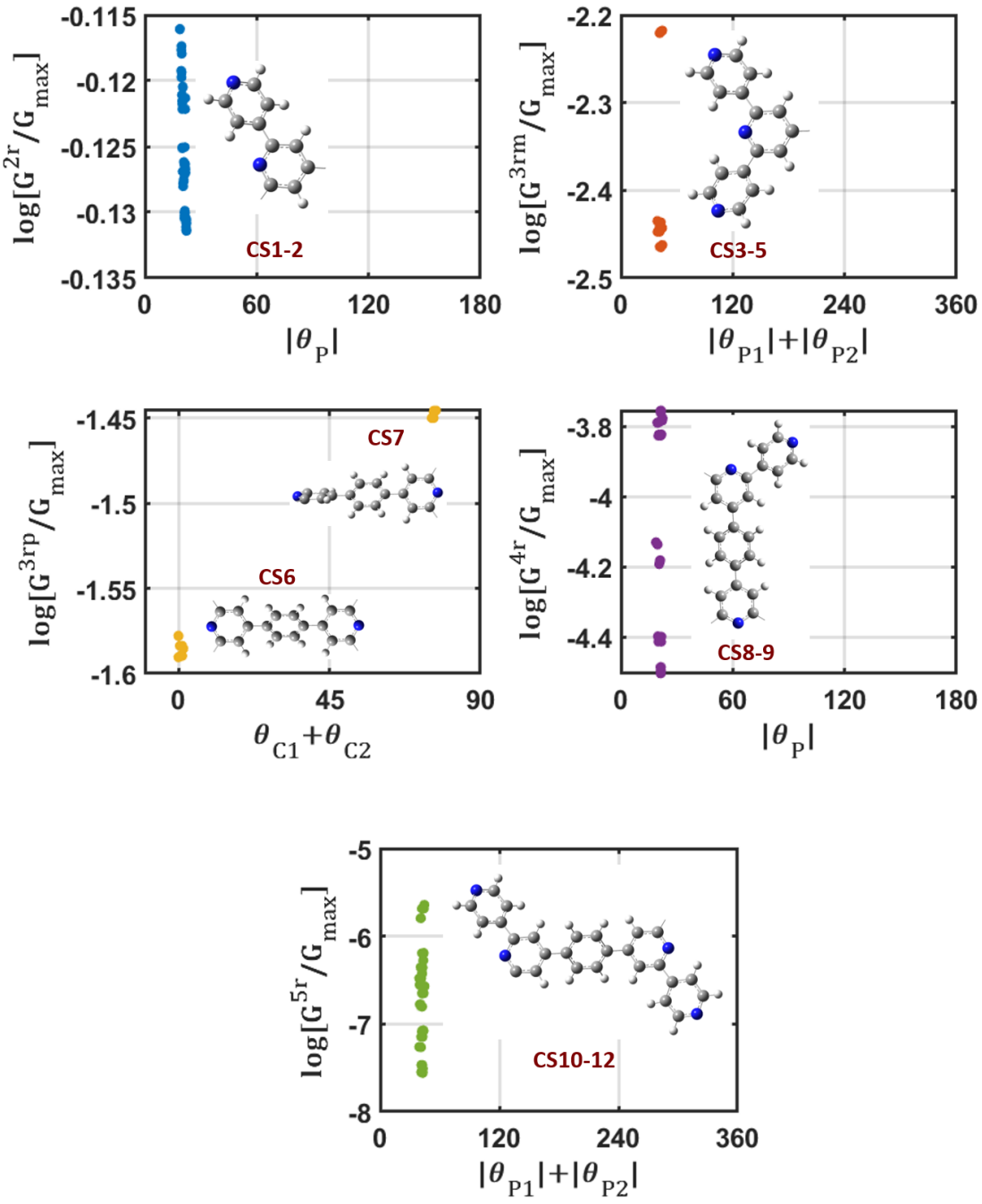


**Fig. S7:** Scatter plots for the logarithmic conductance of 5 basis circuits in all the distinct conformations of TPp. For TPp, due to para placement of peripheral N-atoms, each of 5 basis circuits exist in its single conformational state (except 3rp circuit). The logarithmic conductance is plotted as function of composite angles which is defined in Fig. S6 (conformational state for the basis circuit).

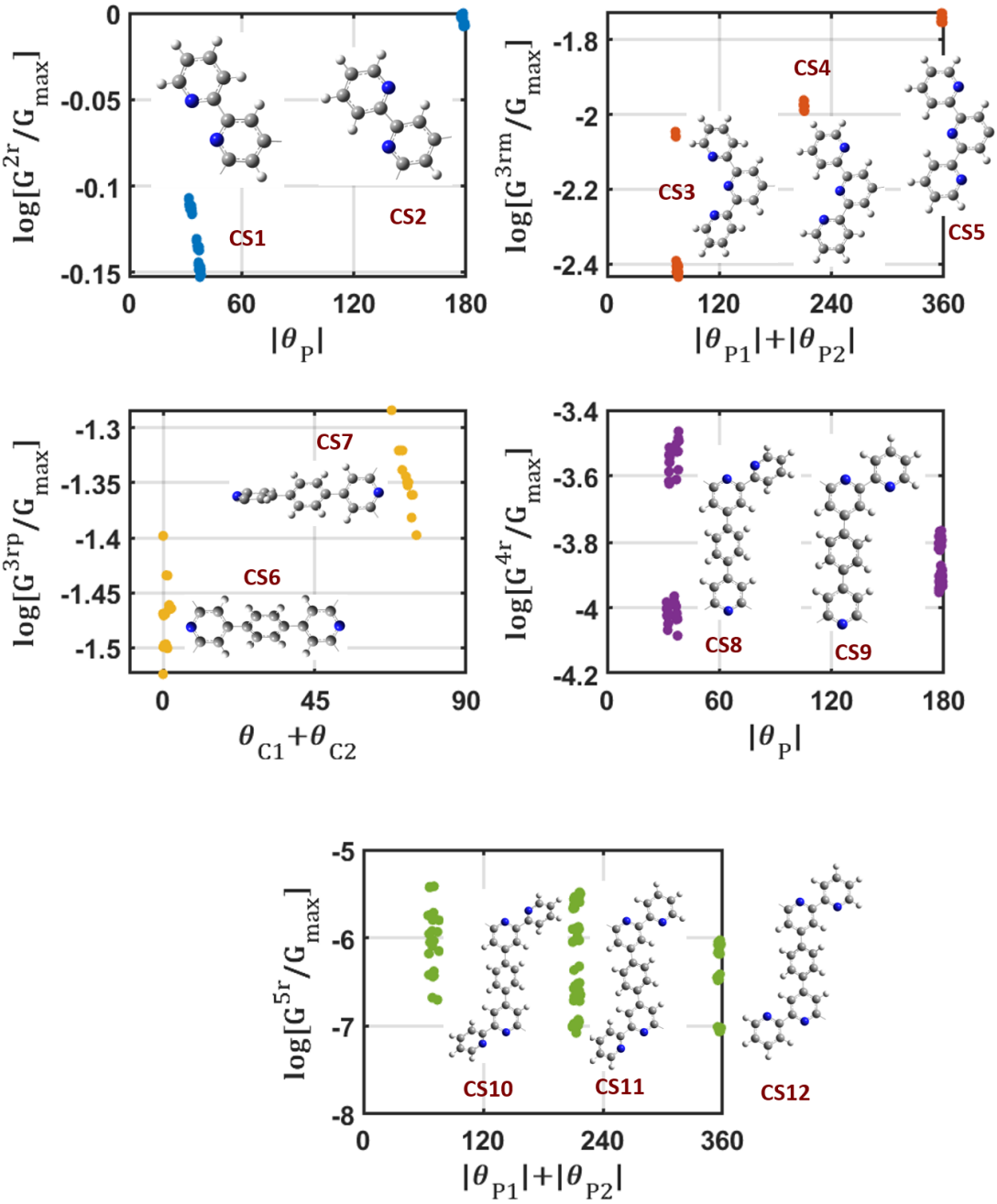


**Fig. S8:** Scatter plots for the logarithmic conductance of 5 basis circuits in all the distinct conformations of TPo. The logarithmic conductance is plotted as function of composite angles which define conformational state for a particular basis circuit. The composite angle is related to in and out conformations of peripheral N-atoms (section S2) in case of 2r, 3rm, 4r, and 5r circuits while it is related to angle between the core pyridyl rings in case of 3rp. The corresponding conformational states for basis are shown inside the plot. The multiple conductance states for basis circuits correlate well with the conformational states. However, for a few circuits multiple peaks are not resolved (for instance, 5r circuit). Furthermore, circuits in TPo shows multiple conductance states corresponding to single conformational state (3rm and 4r circuits). $\theta_P$, $\theta_{P1}$, $\theta_{P2}$, $\theta_{C1}$, and $\theta_{C2}$ are the dihedral angles for the corresponding circuit where P and C denotes the peripheral and core angles.

## S.5 End-to-end Basis Circuit lengths in TPx Breadboards

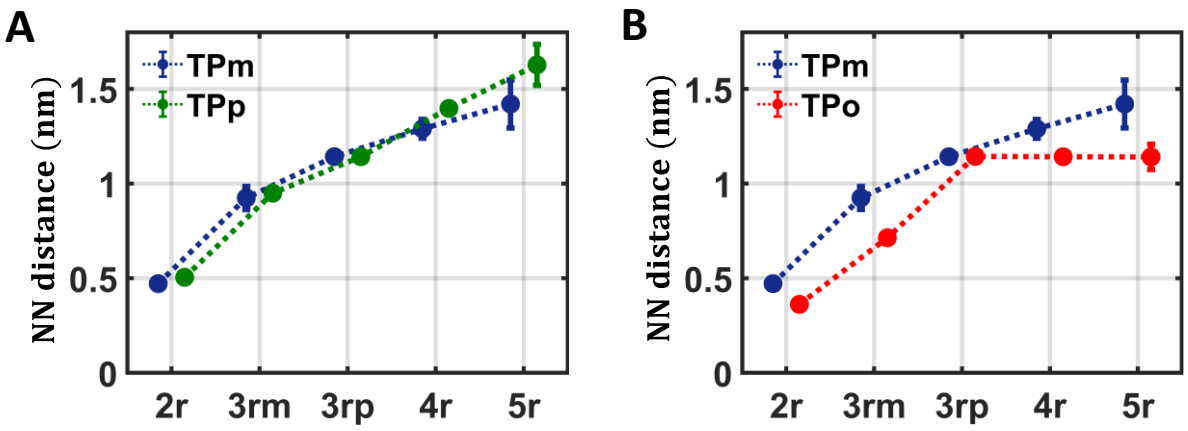


**Fig. S9:** End-to-end distance averaged over molecular conformations for (**A**) TPm and TPp, (**B**) TPm and TPo.

## S.6 Decomposition of transmission into pure and interference terms

To demonstrate multi-orbital constructive and destructive quantum interference on simpler benzene system, we first discuss a simple case wherein the Hamiltonian is given by Hückel model and Fermi level ($E_f$) is placed at the band gap center. Subsequently, we discuss QIE with a more realistic INDO/s Hamiltonian for benzene and wherein $E_f = -5.1eV$ is not placed at band gap center. Finally, the analysis demonstrated for benzene is used to describe multi-orbital DQI for all the basis circuits in TPx breadboards. In the main manuscript, the DQI for a 2r circuit in TPx breadboards is explained. Fig. S10 shows the pure contributions from molecular orbitals (MOs), interference between pairs of MOs, and the multi-orbital QIE for both the Hamiltonians— Hückel and INDO/s—for benzene when connected to electrodes at ortho, meta and para positions. The $Q$–factor analysis[4] and multi-orbital QIE are described in main manuscript (Methods subsection 5.3). For the simple Hückel model, there are only six molecular orbitals wherein the two filled (HOMO and HOMO') and two unfilled (LUMO and LUMO') orbitals are nearly degenerate.[4] It is evident from the heatmaps in Fig. S10A–C that major contributions come from the constructive (ortho and para connected benzene) and destructive (meta connected benzene) QIE between one of the two nearly degenerate HOMOs and one of the two nearly degenerate LUMOs. Nonetheless, all the three systems show CQI as

well as DQI among the MOs. To analyze the overall effect of multi-orbital QIE, we plot cumulative $\mathcal{Q}$-matrix elements in Fig. S10D–F. The cumulative sum of the off-diagonal elements ($\mathrm{X}(n=6)=\sum_{i,j<i}^{6}(\mathcal{Q}_{ij}+\mathcal{Q}_{ji})$ in Fig. S10D–F) indicates that ortho and para connected benzene show overall CQI ($\mathrm{X}(n=6)>0$); on the other hand, the meta connected benzene exhibits overall DQI ($\mathrm{X}(n=6)<0$). The net effect of QIE is that conductance of ortho and meta connected benzene are higher than that of meta connected benzene (see $\mathrm{Z}(n=6)$ in Fig. S10D–F). Next, we move our attention to more realistic benzene system described by INDO/s Hamiltonian and electrode Fermi energy placed at $-5.1eV$. For the INDO/s Hamiltonian, there are only 10 MOs (out of 30) that show significant pure contributions and interfere with each other (Fig. S10G–L). In this case as well, dominant contributions arise from the CQI (ortho/para connected benzene) and DQI (meta connected benzene) between one of the two nearly degenerate HOMOs and one of the two nearly degenerate LUMOs. For the INDO/s Hamiltonian of benzene, the multiorbital interference patterns reveals that only the ortho system exhibits CQI ($\mathrm{X}(n=30)>0$ in Fig. S10J); while meta and para system exhibit DQI ($\mathrm{X}(n=30)<0$ in Fig. S10K–L). Nonetheless, extent of DQI in para connected benzene is very low *i.e.* $\mathrm{X}(n=30)$ is small relative to $\mathrm{Y}(n=30)$ in Fig. S10L. Overall, differing extents of multi-orbital QIE lead to much higher conductance for ortho and para connected benzene relative to meta connected benzene ($\mathrm{Z}(n=30)$ in Fig. S10J–L). The framework described for benzene is applied to TPx breadboards to interpret the boosts and suppressions in conductance of basis circuits within and across breadboards. Fig. S11 shows that there is overall muti-orbital DQI ($\mathrm{X}(n=192)<0$) for all the basis circuits in three TPx breadboard systems (single instances of basis circuits from the most thermally accessible conformation of a particular breadboard molecule have been shown). Asymmetry between the cumulative pure $\sum_i \mathcal{Q}_{ii}$ and interference $\sum_{i,j<i}(\mathcal{Q}_{ij}+\mathcal{Q}_{ji}$ terms about cumulative $\mathcal{Q}_{ij}=0$ line (in each panel of Fig. S11) determines the extent of DQI and final conductance of basis circuits. Further, the total transmission is dominated by strong pure and interference contributions from MOs 80–100 for the TPx systems (data between two black vertical lines in Fig. S11).

Figs. S12–14 show the full heatmap to visualize the pure and interference contributions between the pairs of MOs for a 2r circuit in the thermally most accessible conformations of TPm, TPp, and TPo. While both DQI and CQI are present between the MOs for a 2r circuit as shown in Figs. S12–14, the overall interference is DQI. The DQI between a pair of MOs originates from either change in amplitude sign of the orbital on N-atoms plus/or the lower electron density on the N-atoms as described in main manuscript.

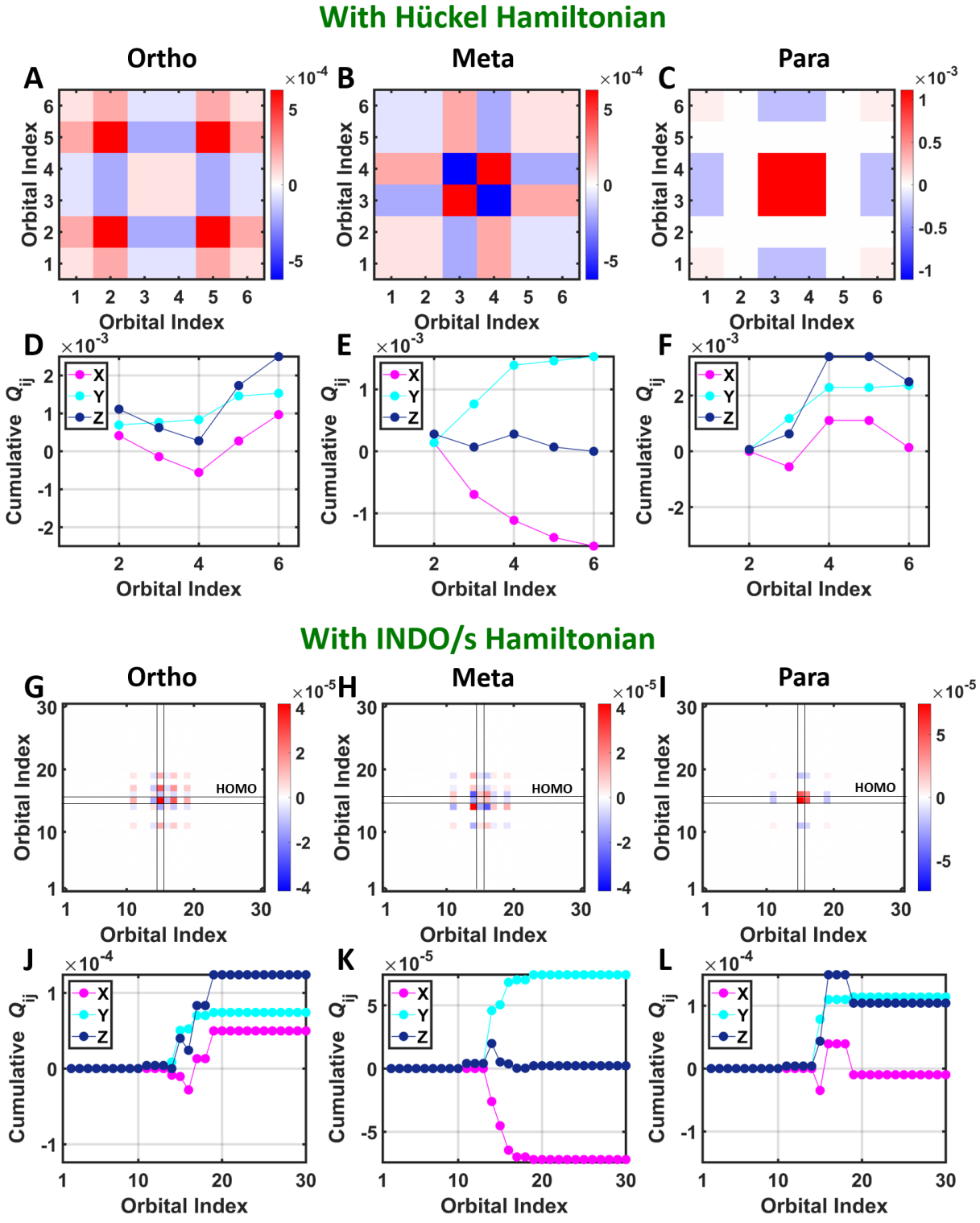


**Fig. S10:** (**A**–**C** and **G**–**I**) Heatmaps for ortho/meta/para connected benzene to visualize the pure and interference terms using Hückel and INDO/s Hamiltonian. (**B**) and (**C**) have been reproduced from ref 4. (**D**–**F** and **J**–**L**) Cumulative (sum over orbitals) $\mathcal{Q}$-matrix elements for ortho/meta/para connected benzene to demonstrate the multi-orbital QIE. Here, cumulative diagonal $\mathrm{Y}(n) = \sum_i^n \mathcal{Q}_{ii}$ (cyan), off-diagonal $\mathrm{X}(n) = \sum_{i,j<i}^n (\mathcal{Q}_{ij} + \mathcal{Q}_{ji})$ (magenta), and the overall transmission $\mathrm{Z}(n) = \mathrm{X}(n) + \mathrm{Y}(n)$ (blue) is plotted. $E_f = 0$ (band gap center) for Hückel Hamiltonian and $E_f = -5.1eV$ for INDO/s Hamiltonian.

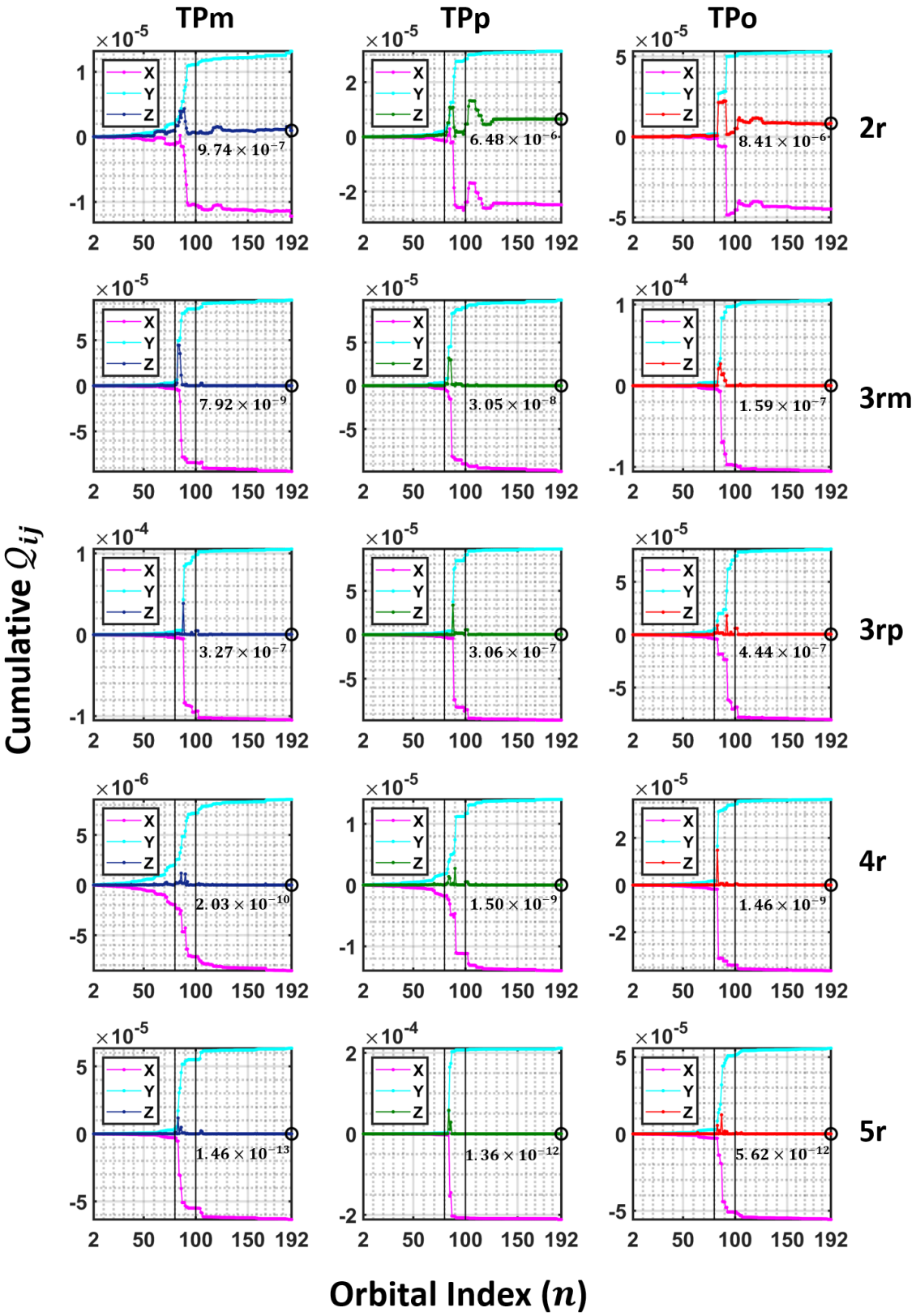


**Fig. S11:** Cumulative diagonal terms $\mathrm{Y}(n) = \sum_i^n \mathcal{Q}_{ii}$ (magenta points), off-diagonal terms $\mathrm{X}(n) = \sum_{i \neq j}^n \mathcal{Q}_{ij}$ (cyan points), and the overall cumulative current $\mathrm{Z}(n) = \mathrm{X}(n) + \mathrm{Y}(n)$ for 5 basis circuits of highest thermally accessible conformation (blue/green/red points for TPm/p/o respectively). REA effects are not considered here (all N/C atoms have equal electrode accessibilities).

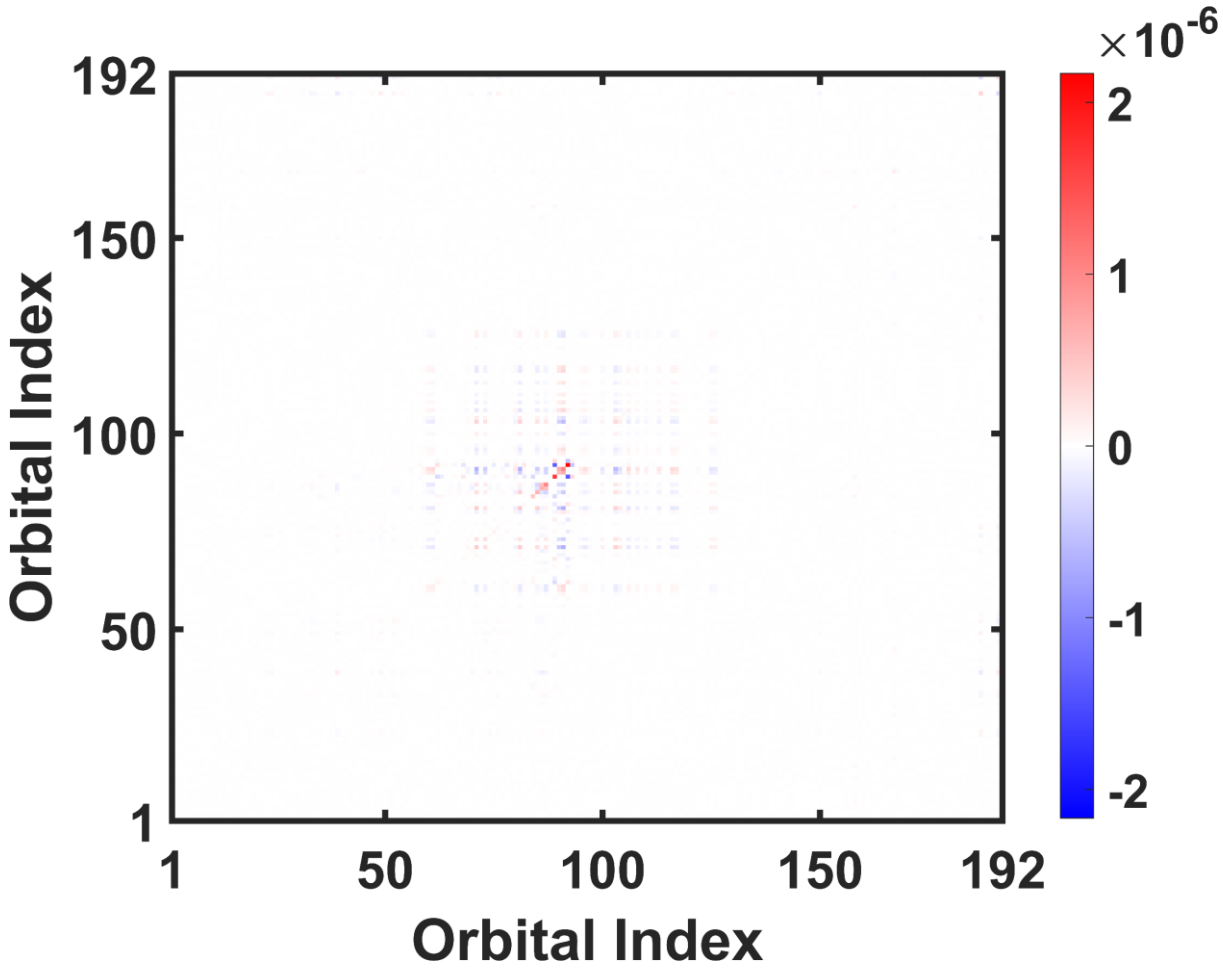


**Fig. S12:** Heatmap for all the MOs showing pure and interference terms between pairs of CMOs for 2r circuit in TPm wherein contributions for MO80–100 has been shown in main text Fig. 3D.

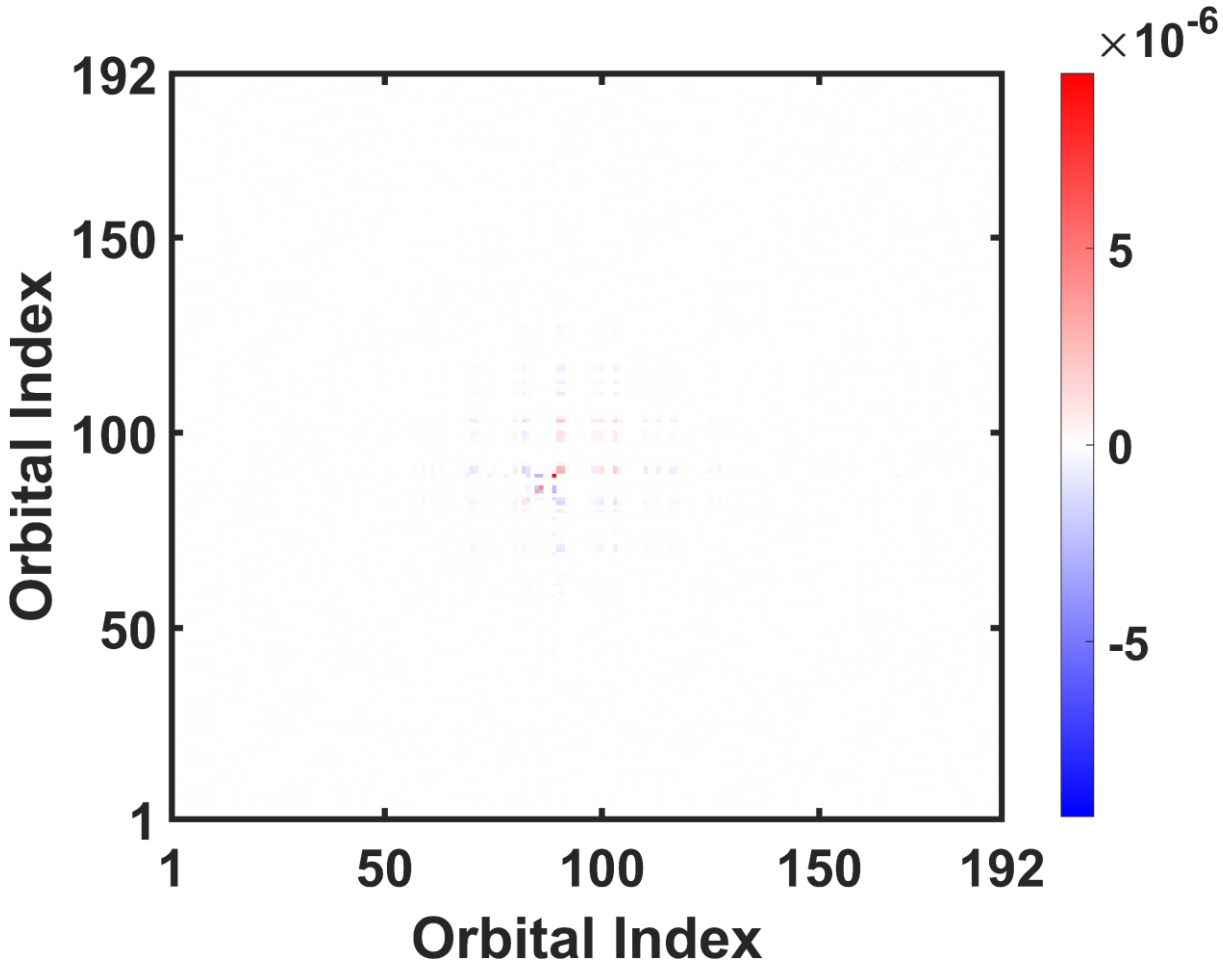


**Fig. S13:** Heatmap for all the MOs showing pure and interference terms between pairs of CMOs for 2r circuit in TPp wherein contributions for MO80–100 has been shown in main text Fig. 3E.

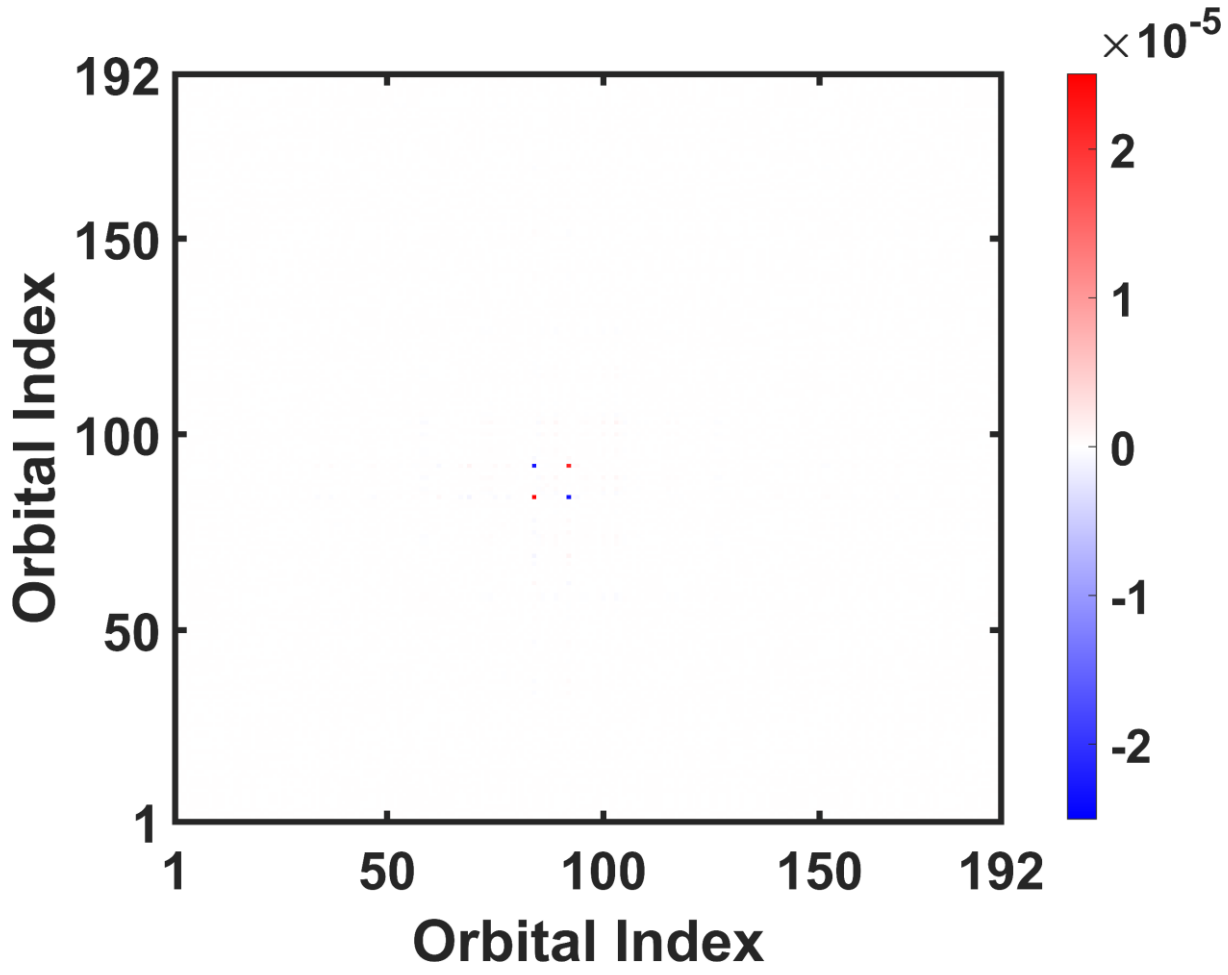


**Fig. S14:** Heatmap for all the MOs showing pure and interference terms between pairs of CMOs for 2r circuit in TPo wherein contributions for MO80–100 has been shown in main text Fig. 4C.

## S.7 Solvent Accessible Surface Area of N-atoms in TPx Breadboards

Fig S15 shows the solvent accessible surface area (SASA) for all the anchoring atoms in the 3 breadboard molecules. SASA is computed by rotating a single gold atom with van der Waals radius of 1.66Å around the nitrogen anchoring groups in breadboards restricted by rest of the molecule. Clearly, SASA for core N-atoms across TPm/o/p is similar (slightly higher for TPo) indicating almost similar REA for the core N-atoms across three breadboards. However, SASA for peripheral N-atom in TPo molecule is lower relative to TPm/p, while peripheral N-atoms in TPm and TPp show similar SASA values. That is why, REA for peripheral N-atoms in the TPo is lower that of TPm/p which subsequently affects the conductance of basis circuits in the 3 breadboards (see Results in main text). Brown data point in Fig. S15 represents the SASA for ortho-placed carbon atoms within the TPm breadboard with peripheral dihedral angle of ~19-26° relative to ~0-3° in TPo (Fig. S4). Thus, the accessibility of the N-atoms in TPo should increase with increase in the peripheral dihedral angles (different conformations). Based on these calculations we assume that the electrode can freely coordinate with peripheral ring meta/para N atoms but is sterically occluded from contacting peripheral ring ortho N atoms and the core ring N atom.

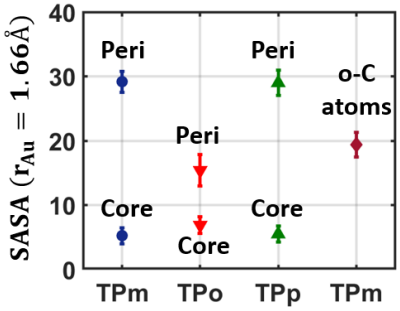


**Fig. S15:** Solvent accessible surface area (SASA) of peripheral and core linking N-atoms in TPm, TPo, and TPp. SASA value for ortho carbon atom of TPm molecule (brown point) indicates increase in SASA for peripheral N-atom in TPo with the peripheral dihedral angle. van der Waals radius for Au atom was taken as 1.66Å.

## S.8 Transferability of REA model to systems other than TPx

Here, we demonstrate that the REA model we developed is not limited to the TPx breadboards only, but is applicable for other molecular junctions as well. We choose a simpler variation of the widely studied oligo(phenyleneethynylene) (OPEs) systems (Fig. S16) and calculate the REA for anchoring atoms using the procedure described in Methods subsection 5.4. The REA data ($\alpha$ values) for three systems in Fig. S16 is provided in Table S2.

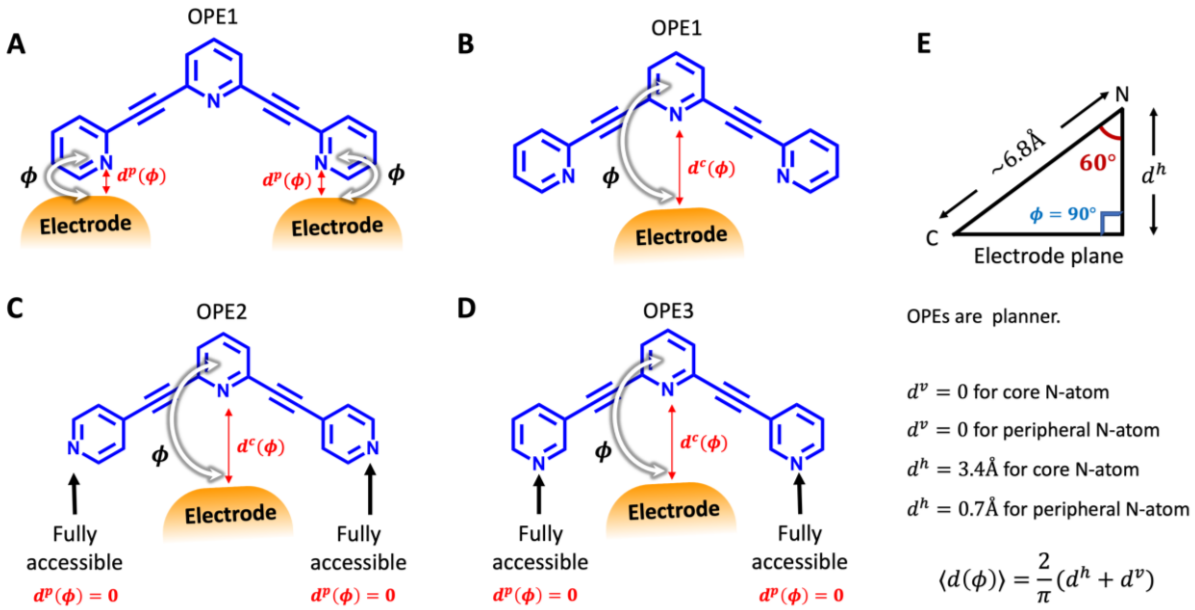


**Fig. S16:** Modified OPE molecules and corresponding screening distances. (**A–B**) OPE1 has both the N-atoms less accessible to the electrodes, (**C–D**) OPE2 and OPE3 molecules have fully electrode accessible N-atoms as well as less accessible N-atom. In (**E**), we show the calculation of $d^h$ for core atom. Similarly, $d^h$ for peripheral N-atom in OPE1 can be calculated.

**Table S2:** Screening distances as a function of the tilt angle $\phi$ and the corresponding attenuation factors ($\alpha$) for peripheral ($p$) and core ($c$) N-atoms in the modified OPEs (Fig. S10). The average bond length $b_1 = 1.40$Å and $b_2 = 1.2$Å for the C=C and C≡C bonds, respectively in the modified OPEs.

| **Molecule** | $\boldsymbol{d^p(\phi)}$[(a)] | $d^p_{eff}$(Å) | $\boldsymbol{\alpha_p}$[(b)] | $\boldsymbol{d^c(\phi)}$[(a)] | $d^c_{eff}$ | $\boldsymbol{\alpha_c}$[(b)] |
|---|---|---|---|---|---|---|
| OPE1 | $\frac{1}{2}b_1 sin\phi$ | 0.45 | 0.26 | $(4b_1 + b_2)sin\phi$ | 2.16 | $1.5 \times 10^{-3}$ |
| OPE2 | 0 | 0 | 1 | $(4b_1 + b_2)sin\phi$ | 2.16 | $1.5 \times 10^{-3}$ |
| OPE3 | 0 | 0 | 1 | $(4b_1 + b_2)sin\phi$ | 2.16 | $1.5 \times 10^{-3}$ |

(a) For core N-atom, $d(\phi) = d^v cos\phi + d^h sin\phi$ is same for OPEs. Note that OPEs systems are planner; therefore, averaging over molecular conformations is not required. Further, $d^v = 0$ and $d^h = 3.4$Å.

(b) Attenuation factors computed as $\alpha = \exp(-\beta d_{eff})$ and $d_{eff} = \langle d(\phi) \rangle_\phi$. The brackets $\langle\ \rangle_\phi$ represent an averaging over the tilt angle $\phi$ as given by Eqn. 10.

## S.9 Conductance of Basis Circuits

**Table S3**: $\langle \log(G/G_{3rp}^{TPm}) \rangle$ given by Eqn. 13 and standard deviations in $\log(G/G_{3rp}^{TPm})$ over molecular conformations (Eqns. 14 and 15) for 5 basis circuits in TPx breadboards. Conductance values are normalized with respect to 3-ring para circuit conductance in TPm.

| Basis Circuit | TPm | | TPo | | TPp | |
|---|---|---|---|---|---|---|
| | $\langle \log(G/G_{3rp}^{TPm}) \rangle$ | Standard deviation | $\langle \log(G/G_{3rp}^{TPm}) \rangle$ | Standard deviation | $\langle \log(G/G_{3rp}^{TPm}) \rangle$ | Standard deviation |
| **2r** | 2.58 | 0.06 | 3.25 | 0.01 | 3.44 | 0.01 |
| **3rm** | 2.37 | 0.43 | 2.72 | 0.00 | 3.23 | 0.11 |
| **3rp** | 0.00 | 0.07 | 0.76 | 0.05 | 0.00 | 0.07 |
| **4r** | -1.09 | 0.17 | -0.54 | 0.05 | -0.49 | 0.31 |
| **5r** | -2.12 | 0.29 | -1.91 | 0.28 | -1.08 | 0.57 |

## S.10 Incoherent Contributions to the Basis Circuit Conductance

We use Landauer-Büttiker probe (LBP) method to investigate the decoherence effects (incoherent current) in the charge transport through five basis circuits in TPx breadboards. In LBP method, the incoherent effects are included in phenomenological manner. The LBP method is described elsewhere.[5,6] To incorporate the phase decoherence effects, molecular sites are coupled to the probe electrodes which can exchange particles. The Büttiker probes absorb current from the molecular bridge and re-inject it to the bridge with a random phase. However, for TPx molecules, identifying the orbitals to attach to the probe reservoirs presents a challenge. From the analysis of the decomposed current, it is evident that orbitals near HOMO and LUMO are major contributors to the overall conduction through the basis circuits (see subsections 2.2 and 2.3 in main manuscript and section S.6 in the ESI). These majorly contributing MOs are $\pi$-character dominated, formed by $p_z$ orbitals of C/N atoms in the three molecules. Therefore, we connect Büttiker probes to each of the $p_z$ orbital of C/N atoms, thus, a total of 42 probes getting attached to each of TPx molecules. The Green`s for the system is given by:

$$\mathcal{G}(E) = \left[ EI - H - \left( \Sigma_{\mathrm{L}} + \Sigma_R + \sum_{P=1}^{42} \Sigma_P \right) \right]^{-1} \tag{S8}$$

here, $\Sigma_P$ is the self-energy associated with the probe electrodes and the other terms are described in the main manuscript (Eqn. 6). The current re-injected from $p^{\text{th}}$ Büttiker probe can travel to any of the reservoirs—$L$, $P = 1,2,3 \cdots p-1, p+1, \cdots 42$, and $R$—through independent coherent channels. The total net current that reaches the $R$ electrode can be given by:

$$I_R = \frac{2q}{h} \int dE \left[ \mathcal{T}_{LR}(E)[f_L(E) - f_R(E)] + \sum_{P=1}^{42} \mathcal{T}_{PR}(E)[f_P(E) - f_R(E)] \right] \quad \text{(S9)}$$

where the transmission function $\mathcal{T}_{PQ}(E)$ is given by:

$$\mathcal{T}_{PQ}(E) = Tr[\Gamma_P \mathcal{G} \Gamma_Q \mathcal{G}^\dagger] \quad \text{(S10)}$$

wherein $\Gamma_P = i(\Sigma_P - \Sigma_P^\dagger)$, the broadening matrix for $P^{\text{th}}$ probe electrode has elements:

$$\begin{aligned} (\Gamma_P)_{ii} &= \gamma_P \quad \text{(For } p_z \text{ orbital of C/N atom corresponding to } P^{\text{th}} \text{ probe electrode)} \quad \text{(S11)} \\ &= 0 \quad \text{(For all other orbitals)} \\ (\Gamma_P)_{ij} &= 0 \quad \text{(For } i \neq j\text{)} \end{aligned}$$

here, $\gamma_P$ is the coupling strength between the $p_z$ orbital of C/N atom and the $P^{\text{th}}$ probe electrode. The broadening matrix elements for $L$ and $R$ electrodes are given by Eqn. 7 in the main manuscript. We scan the value of $\gamma_P$ from $10^{-10}$ to $10^{-1}$ for each basis circuits in TPx breadboards to analyze the conductance as a function of probe coupling. The Fermi functions for $L$ and $R$ electrodes are defined in main manuscript (Eqn. 4) and given by their corresponding chemical potentials. The Fermi functions $f_{P1}$–$f_{P42}$ are unknown and determined from the constraint that at energy $E$ each Büttiker probe electrode absorbs zero net current:

$$\begin{aligned} I_P(E) = 0 = \mathcal{T}_{LP}(E)[f_L(E) - f_P(E)] + \mathcal{T}_{RP}(E)[f_R(E) - f_P(E)] \\ + \sum_{P'=1, P' \neq P}^{42} \mathcal{T}_{P'P}(E)[f_{P'}(E) - f_P(E)] \end{aligned} \quad \text{(S12)}$$

By solving these 42-coupled linear equations for a varying range of $\gamma_P$, we obtain that the Fermi function for each of 42 probes at the energy $E$ lies between the $f_L(E)$ and $f_R(E)$ values. Tails of the broadened energy levels overlap with the energy window for electron transfer (between $f_L(E)$ and $f_R(E)$) and lead to hopping of the electron from $L$ electrode to the molecular orbitals.

With all of these Fermi functions, the total current is calculated using Eqn. S9. In Figs. S16A–C, we compare the incoherent conductance contributions of the five basis circuits (conductance with Büttiker probe attached) in each TPx breadboard with the coherent conductance (with no Büttiker probe attached) as a function of $\gamma_P$. Consistent with earlier observations,[5,6] it is evident from Fig. 17A–C that a shorter circuit—2r is shortest—shows tunneling to hopping crossover at larger value of $\gamma_P$ as compared to that of longer circuit—5r is longest. In Fig. S17D–F, we plot the total conductance (coherent + incoherent) for five basis circuits in TPx breadboards as

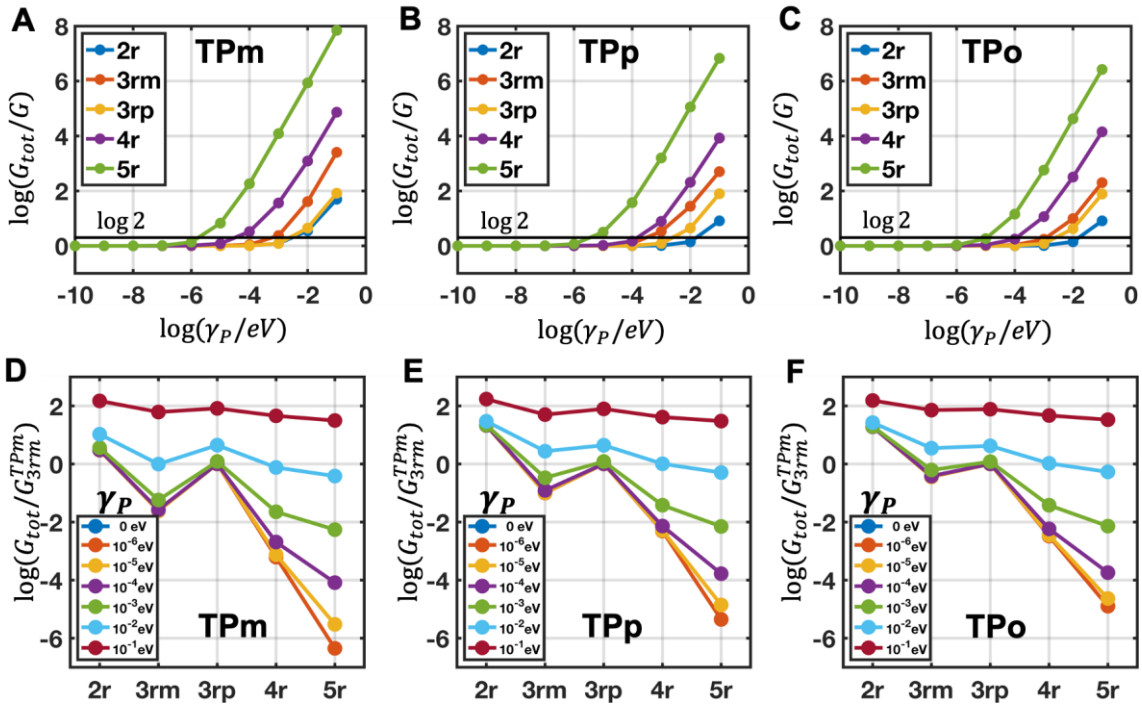


**Fig. S17:** (**A**–**C**) Logarithm of the ratio of the total conductance (coherent + incoherent) to the coherent conductance of the five basis circuits. The horizontal black line indicates a ratio wherein the coherent and incoherent conductance are equal ($G_{tot} = 2 \times G$). Any point on the black horizontal line represents equal contributions from coherent and incoherent conductance to the overall conductance of basis circuit. (**D**–**F**) Basis circuit conductance (coherent + incoherent) as function of probe coupling $\gamma_P$ for TPm, TPp, and TPo respectively. The conductance for $\gamma_P = 0$ and $10^{-6}eV$ conincide.

a function of $\gamma_P$. For small values of $\gamma_P$ ($< 10^{-5}eV$), the conductance trends do not change significantly. On the other hand, for large $\gamma_P$ values (0.01 or 0.1 $eV$), the QIE-induced basis circuit conductance trends are washed out and conductance of all the basis circuits spans only $\leq 1$ order of magnitude. In this case, conductance is dominated by hopping transport such that once an electron occupies a molecular orbital, it spends enough time to be extracted from any of the N atoms of the breadboard scaffold which leads to comparable currents for all of the basis circuits. Therefore, incoherent effects can modulate the basis circuit conductance to a

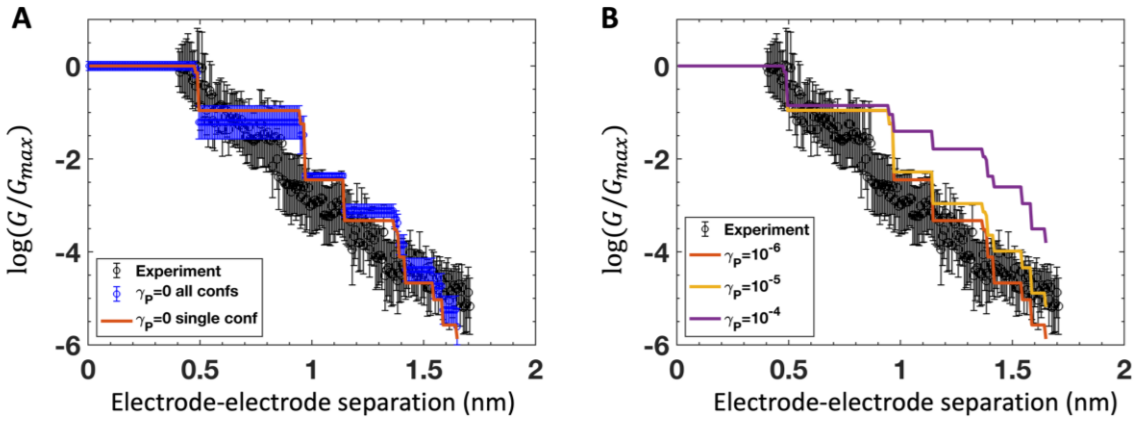


**Fig. S18:** Total conductance (coherent + incoherent) for the TPm breadboard junction as function of dephasing parameter $\gamma_P$. (**A**) Three conductance traces as a function of distance obtained from: (1) MCBJ experiments (black), (2) computations using all the conformations at $\gamma_P = 0$ (blue), and (3) computations using the most thermally accessible conformation at $\gamma_P = 0$ (red). Note that the conductance for a single (most thermally accessible) conformation (red line) was found to be the lowest among all conformations (blue line) at longer electrode-electrode separations where dephasing effects are most prominent. (**B**) Fits to experiments using our computational framework with different $\gamma_P$ values and the most thermally accessible conformation. The lowest $\gamma_P = 10^{-6}eV$ corresponds to the conductance with zero dephasing as shown in Fig. R1. For $\gamma_P = 10^{-5}eV$, the fits worsen (note that the yellow line is the lower bound of the conductance at longer electrode-electrode separations) and grow progressively poorer for large $\gamma_P$ values.

large extent for sufficiently large values of the dephasing parameter ($\gamma_P$) so that conductance for all the basis circuit span only one order of magnitude (rather than > 5 orders of magnitude). This analysis shows that signatures of incoherent charge transport processes in the relative conductance trends only manifest for $\gamma_P$ values $> 10^{-5}eV$ with the conductance of longer basis circuits (4r and 5r) impacted first. However, fits to experimental data for TPm from our previous study[7] and presented here in Fig. S18 reveal that the $\gamma_P$ values cannot exceed $10^{-6}eV$ with fits progressively getting worse with increasing $\gamma_P$. Thus, based on the barriers and distances (see Methods subsection 5.3) for charge transport in the TPx systems and fits to experimental data for TPm (see Fig. S18), we predict that incoherent transport contributions are not significant.

## References:

(1) Wu, J.; Ning, H.; Xu, X.; Ren, W. Accurate Entropy Calculation for Large Flexible Hydrocarbons Using a Multi-Structural 2-Dimensional Torsion Method. *Physical Chemistry Chemical Physics* **2019**, *21* (19), 10003–10010. https://doi.org/10.1039/c9cp00191c.

(2) Chan, L.; Morris, G. M.; Hutchison, G. R. Understanding Conformational Entropy in Small Molecules. *J Chem Theory Comput* **2021**, *17* (4), 2099–2106. https://doi.org/10.1021/acs.jctc.0c01213.

(3) Frisch, M. J.; Trucks, G. W.; Schlegel, H. B.; Scuseria, G. E.; Robb, M. A.; Cheeseman, J. R.; Scalmani, G.; Barone, V.; Mennucci, B.; Petersson, G. A.; Nakatsuji, H.; Caricato, M.; Li, X.; Hratchian, H. P.; Izmaylov, A. F.; Bloino, J.; Zheng, G.; Sonnenberg, J. L.; Hada, M.; Ehara, M.; Toyota, K.; Fukuda, R.; Hasegawa, J.; Ishida, M.; Nakajima, T.; Honda, Y.; Kitao, O.; Nakai, H.; Vreven, T.; Montgomery, J. A., Jr.; Peralta, J. E.; Ogliaro, F.; Bearpark, M.; Heyd, J. J.; Brothers, E.; Kudin, K. N.; Staroverov, V. N.; Keith, T.; Kobayashi, R.; Normand, J.; Raghavachari, K.; Rendell, A.; Burant, J. C.; Iyengar, S. S.; Tomasi, J.; Cossi, M.; Rega, N.; Millam, J. M.; Klene, M.; Knox, J. E.; Cross, J. B.; Bakken, V.; Adamo, C.; Jaramillo, J.; Gomperts, R.; Stratmann, R. E.; Yazyev, O.; Austin, A. J.; Cammi, R.; Pomelli, C.; Ochterski, J. W.; Martin, R. L.; Morokuma, K.; Zakrzewski, V. G.; Voth, G. A.; Salvador, P.; Dannenberg, J. J.; Dapprich, S.; Daniels, A. D.; Farkas, Ö.; Foresman, J. B.; Ortiz, J. v.; Cioslowski, J.; Fox, D. J. Gaussian, Inc., Wallingford CT,. 2013.

(4) Gunasekaran, S.; Greenwald, J. E.; Venkataraman, L. Visualizing Quantum Interference in Molecular Junctions. *Nano Lett* **2020**, *20* (4), 2843–2848. https://doi.org/10.1021/acs.nanolett.0c00605.

(5) Venkatramani, R.; Wierzbinski, E.; Waldeck, D. H.; Beratan, D. N. Breaking the Simple Proportionality between Molecular Conductances and Charge Transfer Rates. *Faraday Discuss* **2014**, *174*, 57–78. https://doi.org/10.1039/c4fd00106k.

(6) Korol, R.; Kilgour, M.; Segal, D. Thermopower of Molecular Junctions: Tunneling to Hopping Crossover in DNA. *Journal of Chemical Physics* **2016**, *145* (22). https://doi.org/10.1063/1.4971167.

(7) Seth, C.; Kaliginedi, V.; Suravarapu, S.; Reber, D.; Hong, W.; Wandlowski, T.; Lafolet, F.; Broekmann, P.; Royal, G.; Venkatramani, R. Conductance in a Bis-Terpyridine

Based Single Molecular Breadboard Circuit. *Chem Sci* **2017**, *8* (2), 1576–1591. https://doi.org/10.1039/c6sc03204d.